



Gas and dust in the TW Hydrae association as seen by the Herschel Space Observatory

P. Riviere-Marichalar, C. Pinte, D. Barrado, W. F. Thi, C. Eiroa, I. Kamp, B. Montesinos, J. Donaldson, J. C. Augereau, N. Huélamo, et al.

► To cite this version:

P. Riviere-Marichalar, C. Pinte, D. Barrado, W. F. Thi, C. Eiroa, et al.. Gas and dust in the TW Hydrae association as seen by the Herschel Space Observatory. *Astronomy & Astrophysics - A&A*, 2013, 555, <10.1051/0004-6361/201321506>. <insu-03617067>

HAL Id: insu-03617067

<https://insu.hal.science/insu-03617067v1>

Submitted on 23 Mar 2022

HAL is a multi-disciplinary open access archive for the deposit and dissemination of scientific research documents, whether they are published or not. The documents may come from teaching and research institutions in France or abroad, or from public or private research centers.

L'archive ouverte pluridisciplinaire **HAL**, est destinée au dépôt et à la diffusion de documents scientifiques de niveau recherche, publiés ou non, émanant des établissements d'enseignement et de recherche français ou étrangers, des laboratoires publics ou privés.



Distributed under a Creative Commons CC BY 4.0 - Attribution - International License

Gas and dust in the TW Hydrae association as seen by the *Herschel* Space Observatory[★]

P. Riviere-Marichalar^{1,5}, C. Pinte², D. Barrado^{1,4}, W. F. Thi², C. Eiroa⁵, I. Kamp⁶, B. Montesinos¹, J. Donaldson⁷,
J. C. Augereau², N. Huélamo¹, A. Roberge⁸, D. Ardila⁹, G. Sandell¹⁰, J. P. Williams¹¹, W. R. F. Dent¹², F. Menard^{2,3},
J. Lillo-Box¹, and G. Duchêne^{2,13}

¹ Centro de Astrobiología – Depto. Astrofísica (CSIC-INTA), ESAC Campus, PO Box 78, 28691 Villanueva de la Cañada, Spain
e-mail: [riviere;barrado]@cab.inta-csic.es

² UJF – Grenoble 1/CNRS-INSU, Institut de Planétologie et d'Astrophysique (IPAG) UMR 5274, 38041 Grenoble, France

³ Laboratorio Franco-Chileno de Astronomía (UMI 3386: CNRS – U de Chile/PUC/U Concepción), Santiago, Chile

⁴ Calar Alto Observatory, Centro Astronómico Hispano-Alemán C/Jesús Durbán Remón, 2-2, 04004 Almería, Spain

⁵ Dep. de Física Teórica, Fac. de Ciencias, UAM Campus Cantoblanco, 28049 Madrid, Spain

⁶ Kapteyn Astronomical Institute, PO Box 800, 9700 AV Groningen, The Netherlands

⁷ Department of Astronomy, University of Maryland, College Park, MD 230742, USA

⁸ Exoplanets and Stellar Astrophysics Lab, NASA Goddard Space Flight Center, Code 667, Greenbelt, MD 20771, USA

⁹ NASA *Herschel* Science Center, California Institute of Technology, MC 100-22, Pasadena, CA 91125, USA

¹⁰ SOFIA – USRA, NASA Ames Research Center, USA

¹¹ Institute for Astronomy, University of Hawaii, Honolulu, HI 96822, USA

¹² ALMA, Avda Apoquindo 3846, Piso 19, Edificio Alsacia, Las Condes, Santiago, Chile

¹³ Astronomy Department, University of California, Berkeley, CA 94720-3411, USA

Received 19 March 2013 / Accepted 10 May 2013

ABSTRACT

Context. Circumstellar discs are the places where planets form, therefore knowledge of their evolution is crucial for our understanding of planet formation. The *Herschel* Space Observatory is providing valuable data for studying disc systems, thanks to its sensitivity and wavelength coverage. This paper is one of several devoted to analysing and modelling *Herschel*-PACS observations of various young stellar associations from the GASPS open time key programme.

Aims. The aim of this paper is to elucidate the gas and dust properties of circumstellar discs in the ~10 Myr TW Hya association (TWA) using new far-infrared (IR) imaging and spectroscopy from *Herschel*-PACS.

Methods. We obtained far-IR photometric data at 70, 100, and 160 μm of 14 TWA members; spectroscopic observations centred on the [OI] line at 63.18 μm were also obtained for 9 of the 14. The new photometry for each star was incorporated into its full spectral energy distribution.

Results. We detected excess IR emission that is characteristic of circumstellar discs from five TWA members, and computed upper limits for another nine. Two TWA members (TWA 01 and TWA 04B) also show [OI] emission at 63.18 μm . Discs in the TWA association display a variety of properties, with a wide range of dust masses and inner radii, based on modified blackbody modelling. Both transitional and debris discs are found in the sample. Models for sources with a detected IR excess give dust masses in the range from ~0.15 M_{\oplus} to ~63 M_{\oplus} .

Key words. stars: formation – astrochemistry – protoplanetary disks – circumstellar matter – zodiacal dust – planetary systems

1. Introduction

We can distinguish several phases in the evolution of circumstellar discs. In the protoplanetary stage, the star actively accretes material from the disc, which is gas-rich and extends up to hundreds of AU from the star. This protoplanetary disc is the birthplace of planets. In the transition phase, the disc forms an inner gap that is largely dust-free (Strom et al. 1989; Najita et al. 2007). The radius of the gap is typically in the range 1–20 AU, and may be the result of interactions between the disc and a planetary body (Lin & Papaloizou 1993). At this stage, the star

may still be accreting, but accretion rates are 10 to 100 times lower than in the protoplanetary phase. Debris discs are older systems that are gas-poor and no longer accreting. The presence of dust in such evolved systems is explained as the result of destructive collisions between planetesimals formed earlier in the protoplanetary phase. In this paradigm, dusty circumstellar discs surrounding stars are signposts for the existence of planetesimals and possibly of planets themselves.

The properties of circumstellar discs have been extensively studied over the past 30 years or so (see recent reviews by e.g. Krivov 2010; Williams & Cieza 2011, and references therein). The Multiband Imaging Photometer for Spitzer (MIPS) was widely used to study the properties of dusty discs in evolved systems (e.g. Bryden et al. 2006; Rebull et al. 2008). The *Spitzer*

[★] *Herschel* is an ESA space observatory with science instruments provided by European-led Principal Investigator consortia and with important participation from NASA.

Infrared Spectrograph (IRS) was also used to characterise dust grains in circumstellar environments (e.g. [Chen et al. 2006](#); [Morales et al. 2009](#); [Oliveira et al. 2011](#)). By fitting models to the spectral energy distribution (SED) of a disc system, the amount of dust, the geometry of the disc, the dust composition, and the grain size distribution can be estimated. Even though the gas dominates the mass in a protoplanetary disc, it is more difficult to study than dust, because H_2 lacks a permanent electric dipole moment, which causes the infrared (IR) pure rotational transitions to be very weak. A further difficulty is that molecules like CO are often optically thick and frozen out in the cold mid-plane of the disc, making them poor tracers of the overall gas content.

The *Herschel* Space Observatory ([Pilbratt et al. 2010](#)) provides new opportunities for studies of circumstellar discs. The Photodetector Array Camera and Spectrometer (PACS) ([Poglitsch et al. 2010](#)) has unprecedented sensitivity and angular resolution in the far-IR, enabling the detection of gas and dust in faint, dusty debris discs in the wavelength range where the cold Kuiper-belt like dust emission peaks (70–200 μm). The smaller beam size of PACS compared with *Spitzer*-MIPS results in a lower rate of confusion with background sources. PACS spectroscopy covers the strong cooling lines of [OI] at 63 μm and [CII] at 158 μm , which provides a powerful probe of the gas in circumstellar discs.

The discovery of several nearby ($\lesssim 100$ pc) young ($\lesssim 20$ Myr) sparse stellar associations or moving groups ([Torres et al. 2003](#), [2006](#)) provides another valuable avenue for studying the evolution of gas and dust in circumstellar discs, because the ages of the stars in these moving groups are relatively well known. In the present paper, we target the TW Hydrae association (TWA, [de la Reza et al. 1989](#)). TWA is one of the closest (56 pc) and youngest moving groups (8–20 Myr, see [Kastner et al. 1997](#); [Stauffer et al. 1995](#); [Soderblom et al. 1998](#); [Hoff et al. 1998](#); [Weintraub et al. 2000](#); [Makarov & Fabricius 2001](#); [Makarov et al. 2005](#); [Barrado y Navascués 2006](#); [de la Reza et al. 2006](#)). The range in ages is due to different age determinations from different authors, although we assume the TWA members are coeval. It is a well known place for studying star and planet formation, and the properties of the TWA circumstellar discs have been extensively studied in other works (e.g. [Low et al. 2005](#)).

Currently there are about 30 bona fide members of the TWA association ([Schneider et al. 2012](#)). Fourteen of them were observed as a part of the *Herschel* open key time programme “Gas in Protoplanetary Systems” (GASPS; [Dent et al. 2013](#)), which aims to study the presence and distribution of gas and dust in circumstellar disc systems around young low- and intermediate-mass stars. GASPS has observed ~ 250 stars within 400 allocated h, covering both photometry and spectroscopy. The sample includes several associations at different ages, from Taurus at 1–3 Myr to Tucana-Horologium at ~ 30 Myr. The targets range from HAcBe stars to T Tauri stars, with spectral types from A0 to M6.

In this study, we discuss our new *Herschel*-PACS photometric and spectroscopic observations of 14 TWA members. Images were obtained at 70 and/or 100, and 160 μm for all 14. Spectral line observations of [OI] at 63 μm and DCO⁺ at 189 μm were obtained for nine of them. We studied the properties of the dust and the geometry of the discs by comparing the observed photometric flux densities with those predicted by simple, modified blackbody models. This paper is one of several studies devoted to the analysis of GASPS data in a systematic framework, with the goal of comparing the *Herschel* photometric and spectroscopic results in different associations and moving groups, and studying the evolution of gas and dust as a function of age.

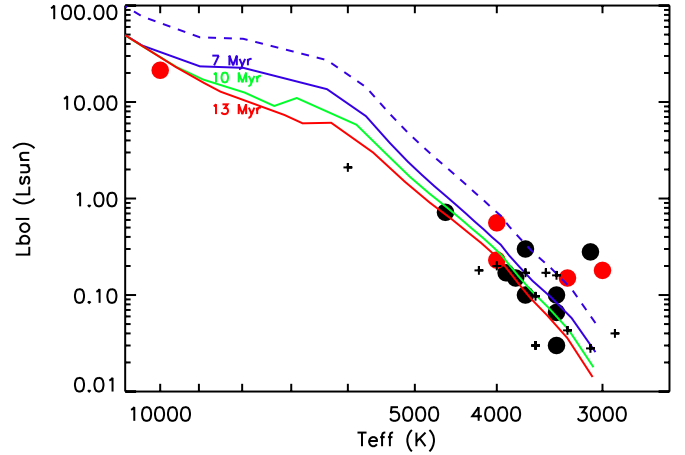


Fig. 1. Hertzsprung-Russell diagram for TWA members in this programme. The red/green/blue solid lines represent the 13/10/7 Myr solar metallicity isochrones from [Baraffe et al. \(1998\)](#). The blue dashed line shows the 7 Myr Baraffe isochrone with 2 times higher luminosity to account for unresolved binary systems. Red dots are objects detected with PACS, while black dots are undetected objects. Plus symbols correspond to TWA members not observed in GASPS.

2. The sample

The sample of 14 TWA members studied in this paper, together with their spectral types (Sp Type), stellar luminosities, and effective temperatures, is shown in Table 1. The spectral types range from A0 to M3. Star distances are taken from [Zuckerman & Song \(2004\)](#). In Fig. 1, we plot the stars on a Hertzsprung-Russell diagram. The stellar luminosities and effective temperatures used are discussed in Sect. 2.1.

Among the sample, TWA 01 ([Salyk et al. 2007](#)), TWA 03A ([Cieza et al. 2008](#)), and TWA 04B ([Furlan et al. 2007](#)) are typically classified as transitional discs, while TWA 07 ([Matthews et al. 2007](#)) and TWA 11A ([Telesco et al. 2000](#)) are believed to be debris discs. It was proposed that TWA 13A harbours a circumstellar disc by [Low et al. \(2005\)](#), but this was later rejected by [Plavchan et al. \(2009\)](#). The eight other systems are not known to harbour any circumstellar disc.

Archival data was collected for each TWA member in our target list, including Johnson, Tycho, 2-Microns All-Sky Survey (2MASS), InfraRed Array Camera (IRAC), Wide-Field Infrared Explorer (WISE), AKARI, Multiband Imaging Photometer for Spitzer (MIPS), Sub-Millimeter Array (SMA) and Submillimetre Common-User Bolometer Array (SCUBA) photometry. *Spitzer*-MIPS values are taken from [Low et al. \(2005\)](#). TWA23 and TWA25 MIPS flux densities are not included in [Low et al. \(2005\)](#). For these two stars, we computed our own photometry for the 24 μm MIPS band, using an aperture of 13 arcsec, and a sky annulus between 20 arcsec and 32 arcsec, and applying the appropriate aperture corrections (as described in the *Spitzer* Data Analysis Cookbook¹). Computed flux densities are 8.6 ± 0.5 mJy for TWA 23 and 10.5 ± 0.5 mJy.

2.1. Stellar parameters

To model the stars’ SEDs, we need knowledge of their stellar properties (specifically, their temperature and luminosity), to choose the correct photosphere models. For each star in the

¹ <http://ssc.spitzer.caltech.edu/dataanalysisistools/cookbook/>

Table 1. Stellar parameters.

Name	Other name	Sp type	Ref	d (pc)	T_{eff} (K)	L_* (L_{\odot})
TWA 01	TW Hya	M2.5	1	56	3400	0.23
TWA 02	CD-29 8887	M2	2	52	3700	0.30
TWA 03A	Hen 3-600	M3	2	42	3000	0.18
TWA 04B	HD 98800B	M5	3	47	4000	0.56
TWA 05A	CD-33 7795	M3	3	50	3100	0.28
TWA 07	CE Ant	M1	4	38	3300	0.15
TWA 10	V1252 Cen	M2.5	4	57	3400	0.10
TWA 11A	HR 4796A	A0	5	67	10 000	21.3
TWA 12	V1217 Cen	M2	6	32	3400	0.03
TWA 13A	V547 Hya A	M2	6	38	3700	0.10
TWA 16	–	M1.5	7	66	3900	0.17
TWA 21	HD 298936	K3	8	69	4600	0.72
TWA 23	–	M1	9	37	3400	0.07
TWA 25	V1249 Cen	M0	9	44	3800	0.15

Notes. All distances are from Zuckerman & Song (2004). T_{eff} and L_* for each target were computed using VOSA (Bayo et al. 2008). References for spectral type (Sp Type) are: (1) Vacca & Sandell (2011); (2) de la Reza et al. (1989); (3) Gregorio-Hetem et al. (1992); (4) Webb et al. (1999); (5) Houk & Fuentes-Williams (1982); (6) Sterzik et al. (1999); (7) Zuckerman et al. (2001); (8) Zuckerman & Song (2004); (9) Weinberger et al. (2004).

sample, we selected the photometric data that do not show excess above the stellar photosphere, i.e. those data points in agreement with pure photospheric emission. Typically, this includes Johnson, Stromgren, and 2MASS data. Then we compared this photospheric emission with a grid of theoretical stellar photosphere models using the Virtual Observatory SED Analyzer (VOSA, Bayo et al. 2008), which provides the best-fitting model based on a χ^2 minimisation. We used the grid of Phoenix models from Hauschildt et al. (1999). The values for T_{eff} and L_* from each best-fitting model are summarised in Table 1.

2.2. Accretion in TWA

The relation between H_{α} emission, a tracer of disc material accreting onto the central star, and [OI] emission can help us understand the gas properties of the TWA members. We took observed H_{α} emission equivalent widths from Barrado y Navascués (2006) and applied the criterion given in Barrado y Navascués & Martín (2003) to classify TWA members as accretors or non-accretors. The accretion criterion accounts for the effect of chromospheric activity, which also gives rise to H_{α} emission.

In Fig. 2, we have plotted the H_{α} emission equivalent widths (EW) versus the spectral types of the stars in the sample, along with the line that separates accretors from non-accretors according to the criterion in Barrado y Navascués & Martín (2003). TWA 01 and TWA 03A show variable H_{α} levels in agreement with an accreting disc. On the other hand, for TWA 05A and TWA 10, only one epoch of data shows an H_{α} equivalent width larger than the expected chromospheric level. We note that these stars show MIPS 24 μm emission consistent with purely photospheric emission, indicating a lack of warm inner material that would be expected for an accreting disc. We therefore conclude that the two high H_{α} observations were due to extremely strong flaring events rather than episodic accretion.

3. Observations and data reduction

The TWA sample was observed with PACS as part of the GASPS open time key programme. Fourteen bona fide TWA members

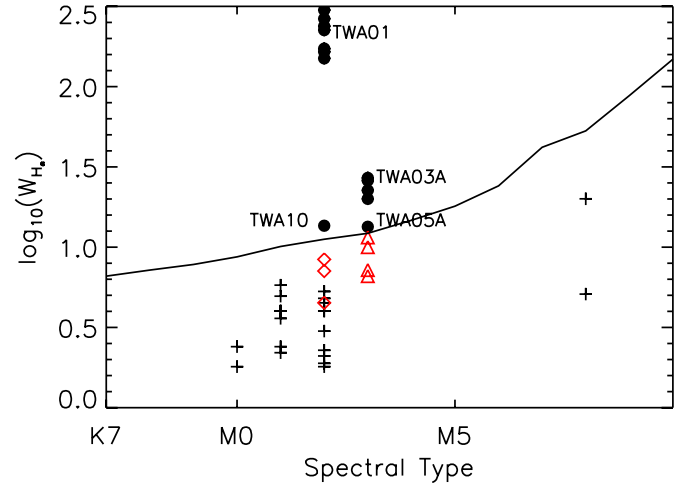


Fig. 2. Accretion in TWA members. Plus symbols depict objects with H_{α} in agreement with pure chromospheric emission, while black dots are objects with H_{α} in agreement with ongoing accretion. TWA 05A and TWA 10 show variable emission with some epochs over the chromospheric level and some epochs below the chromospheric level. Red diamonds and red triangles represent H_{α} equivalent widths below the chromospheric level for TWA 10 and TWA 05A, respectively. The solid line shows the saturation criterion by Barrado y Navascués & Martín (2003).

were observed in photometric mode and a subset of nine TWA members were observed in spectral line mode.

3.1. Photometric data reduction

The PACS photometer simultaneously observes in either the 70 μm or 100 μm bands together with the 160 μm band, so we typically have at least two images to combine in the 160 μm band. PACS scan map observations at 70 μm and 160 μm were obtained for 12 objects. Seven of these objects were also observed at 100 μm and 160 μm . Two additional objects were observed only at 100 μm and 160 μm . Observation IDs are listed in Table 2. The exposure times range from 133 s to 1122 s, based on the expected flux density from the star. Each scan map was made with medium speed (20'' s⁻¹), with scan legs of 3' and cross scan length of 4'' to 5''.

The reduction of the photometric data was carried out using the *Herschel* Interactive Processing Environment (HIPE) 8, with the latest version available for the calibration files. For bright IR sources (i.e., those with flux densities greater than 100 mJy) we used a version of the pipeline tuned for bright objects, while for faint objects and non-detected objects we used a different version optimised for noise-dominated maps, as is the case for TWA 07, among others. The difference between both versions of the pipeline comes from the way in which high-pass filtering is implemented. Before we apply high-pass filtering, we need to mask the sources that we want to study in order to preserve their absolute flux density. For bright sources, we can detect and mask the sources in individual scans before performing the high-pass filtering. For faint sources that cannot be detected in individual scans, a preliminary reduction is run without a high-pass filter, and the final image from this first reduction is then used to mask the source and to run the final reduction with high-pass filtering properly applied.

In both pipelines the reduction process includes the following main steps: bad and saturated pixel flagging and removal,

Table 2. Observation log.

Name	Obs. ID	Obs. Mode
TWA 01	1342187342	ScanMap 70/160
TWA 02	1342189163	ScanMap 70/160
TWA 02	1342211995	ScanMap 70/160
TWA 02	1342211996	ScanMap 100/160
TWA 03A	1342211991	ScanMap 70/160
TWA 03A	1342211992	ScanMap 100/160
TWA 04B	1342188473	ScanMap 70/160
TWA 04B	1342212634	ScanMap 70/160
TWA 04B	1342212635	ScanMap 100/160
TWA 05AB	1342213111	ScanMap 70/160
TWA 05AB	1342213112	ScanMap 100/160
TWA 07	1342188515	ScanMap 70/160
TWA 07	1342211993	ScanMap 70/160
TWA 07	1342211994	ScanMap 100/160
TWA 10	1342188518	ScanMap 70/160
TWA 10	1342213854	ScanMap 70/160
TWA 10	1342213855	ScanMap 100/160
TWA 11	1342188519	ScanMap 70/160
TWA 11	1342213852	ScanMap 70/160
TWA 11	1342213853	ScanMap 100/160
TWA 13	1342213113	ScanMap 70/160
TWA 13	1342213114	ScanMap 100/160
TWA 16	1342188854	ScanMap 70/160
TWA 16	1342213856	ScanMap 70/160
TWA 16	1342213857	ScanMap 100/160
TWA 16	1342213858	ScanMap 70/160
TWA 16	1342213859	ScanMap 100/160
TWA 21	1342188514	ScanMap 70/160
TWA 21	1342211983	ScanMap 70/160
TWA 21	1342211984	ScanMap 100/160
TWA 23	1342188516	ScanMap 70/160
TWA 25	1342188517	ScanMap 70/160
TWA 25	1342213624	ScanMap 70/160
TWA 25	1342213625	ScanMap 100/160
TWA 25	1342213626	ScanMap 70/160
TWA 25	1342213627	ScanMap 100/160

flat field correction, deglitching, high pass filtering, and map projection. Photometric maps were projected onto the final image with pixel scale 2 arcsec/pixel in the 70 μm and 100 μm bands and with pixel scale 3 arcsec/pixel in the 160 μm . We also produced final maps with the native pixel scale of the detector, which were used to perform the error calculation (3.2 arcsec/pixel for the 70 μm and 100 μm bands and 6.4 for the 160 μm band). When several images at the same wavelength were available for a single target, we combined all of them to improve the signal-to-noise ratio (S/N), averaging for each pixel and using the average sigma clipping algorithm to exclude bad pixels.

Aperture photometry was measured in final, combined images using an aperture of 6'' for the 70 and 100 μm bands and 12'' for the 160 μm band. The annulus for sky subtraction was placed at 25–35'' from the star. We then applied the proper aperture correction for each band². The photometric flux densities are listed in Table 3.

To compute photometric errors, we used native maps to minimise the impact of correlated noise, with pixel scale 3.2 arcsec/pixel in the 70 and 100 μm bands and 6.4 arcsec/pixel in the 160 μm band. Noise errors consist on the standard deviation of the photometry obtained at several

Table 3. TWA PACS photometry.

Name	70 μm	100 μm	160 μm
	(mJy)	(mJy)	(mJy)
TWA 01 ¹	3900 \pm 100	–	7380 \pm 300
TWA 03A	–	650 \pm 19	459 \pm 19
TWA 04B	6241 \pm 165	4269 \pm 117	2382 \pm 100
TWA 07	77 \pm 7	58 \pm 4	42 \pm 9
TWA 11	4980 \pm 131	3553 \pm 97	1653 \pm 68
TWA 02	<11.0	<6.4	<19
TWA 05	<2.2	–	<11.0
TWA 10	<4.1	–	<12.0
TWA 12	<2.8	–	<9.0
TWA 13A	–	<6.4	<19.0
TWA 16	<4.4	<4.6	<8.6
TWA 21	<4.0	–	<14.0
TWA 23	<5.1	<6.0	<13.0
TWA 25	<5.7	<6.3	<12.0

Notes. Errors include a calibration error of 2.64%, 2.75% and 4.15% for the 70 μm , 100 μm , and 160 μm bands respectively (see text). Upper limits are 3σ (1): from [Thi et al. \(2010\)](#).

sky positions surrounding the target. PACS calibration errors are 2.64%, 2.75% and 4.15% for the 70 μm , 100 μm and 160 μm bands, respectively³. Noise errors and calibration errors were added quadratically. The impact of correlated noise is negligible: final photometric uncertainties are dominated by the calibration errors, with the only exception of TWA 07.

For non-detected sources, the derivation of upper limits is as follows; we compute the standard deviation in the sky background in several pointing surrounding the nominal position of the star on the detector; then, we compute the average value, and we use it as the sky background value. This value is multiplied by the square root of the number of pixels inside the aperture. Finally, we apply the proper aperture correction. The upper limits included in Table 3 are 3σ .

3.2. Spectroscopic data reduction

Nine TWA stars were observed with PACS in LineScan spectroscopic mode. The line targeted with the LineScan observations was [OI] at 63.18 μm . PACS spectra were reduced using HIPE 8 with the latest version of the pipeline and the proper calibration files.

Spectra were extracted from the central spaxel when the observations were well centred there. When the observations were not properly centred on the source, we extracted the spectrum from the spaxel with the highest continuum signal. The extracted spectrum was then aperture corrected to account for flux loss in the surrounding spaxels. The line spectra from PACS typically show higher noise levels near the spectrum edges. To account for that effect, we exclude from the 63 μm spectra any wavelength shorter than 63.0 μm or longer than 63.4 μm .

Line fluxes were computed by applying a Gaussian fit to the line profile and calculating the integrated flux from that fit. Upper limits were computed by integrating a gaussian with a width equal to the instrumental full width half maximum (FWHM) at the central wavelength, and maximum equal to three times the standard deviation of the continuum. Therefore, computed upper limits are 3σ . Line fluxes are shown in Table 4.

² <http://herschel.esac.esa.int/twiki/pub/Public/PacsCalibrationWeb/>

³ PICC-ME-TN-037.

Table 4. TWA PACS line fluxes.

Name	[OI] _{63.18 μm}	o – H ₂ O _{63.32 μm}	<i>S/N</i> _{63 μm}
–	(10 ^{−18} W/m ²)	(10 ^{−18} W/m ²)	–
TWA 01	36.5 ± 12.1	<2.42	13.3
TWA 02	<8.3	<8.3	0.19
TWA 03A	<5.8	<5.8	33.9
TWA 04B ¹	6.4 ± 1.5	<1.74	41.8
TWA 04B ²	4.0 ± 1.0	<1.34	46.3
TWA 04B ³	4.1 ± 1.2	<1.24	56.9
TWA 07	<4.6	<4.6	1.04
TWA 10	<4.5	<4.5	0.35
TWA 11A	<4.7	<4.7	39.67
TWA 13A	<4.5	<4.5	0.32
TWA 23	<5.4	<5.4	0.28

Notes. Listed values for *S/N* are continuum *S/N*. ⁽¹⁾ OBSID 1342199409. ⁽²⁾ OBSID 1342223821. ⁽³⁾ Averaged spectrum.

4. Results

4.1. *Herschel*-PACS photometry

Within the 12 targets observed at 70 μm, we detected four sources. At 100 μm, we have detected four systems out of nine observed. All the targets detected in the 70 μm and 100 μm bands are also detected at 160 μm, and all of them show emission in excess above the photosphere, in agreement with the presence of circumstellar material. Excess fractions are $0.33^{+0.15}_{-0.10}$, $0.44^{+0.16}_{-0.14}$ and $0.36^{+0.14}_{-0.10}$ at 70 μm, 100 μm and 160 μm, respectively (see Burgasser et al. 2003, for a detailed description of the method used to compute errors on the disc fractions). We have detected for the first time the 100 μm and 160 μm emission toward TWA 07, and 100 μm emission toward TWA 03A.

TWA 13A was considered a far-IR excess source by Low et al. (2005). They found a 27.6 mJy flux density at 70 μm. But Plavchan et al. (2009) showed that the 70 μm emission is coincident with a background galaxy and not with TWA 13A. Our combined images for TWA 13A do not show any source at the nominal position of the star, therefore we agree with Plavchan et al. (2009) that there is no excess associated with TWA 13A. However there is a background galaxy that could have polluted the Low et al. (2005) observation at RA = 11:21:16.6, Dec = −34:46:38.6, with a flux density of 70 mJy at 100 μm and 93 mJy at 160 μm.

In Fig. 3, we show a comparison of the photometry at 70 μm from MIPS with that from PACS for the remaining sources. We see that the agreement between MIPS and PACS for detected objects is good; both datasets are in agreement within the calibration uncertainties, and sources are therefore not variable. Any discrepancy can be due to problems in the calibration of the instruments, to the larger beam size in MIPS or to real variability. The most probable explanation lies on the larger beam size used by MIPS, which can include some contamination from the background. The upper limits from PACS are pushing further down to photospheric values, and are typically ~5 times smaller than previous upper limits from MIPS.

In Fig. 4, we plot the 70 μm, 100 μm and 160 μm excess versus the effective temperature of the central star. The excesses are computed as the observed flux density over the photospheric flux density at each band. Photospheric flux densities are extracted from the models in Sect. 2.1. The behaviour is the same for every PACS band; a system bright at 70 μm is also bright at

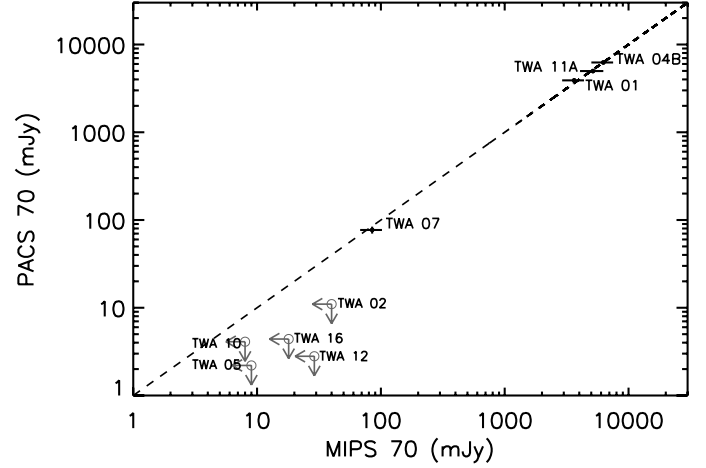


Fig. 3. Comparison plot for PACS 70 μm flux densities vs. MIPS 70 μm flux densities. The black dashed line represents the one to one relation. Displayed upper limits are 3σ.

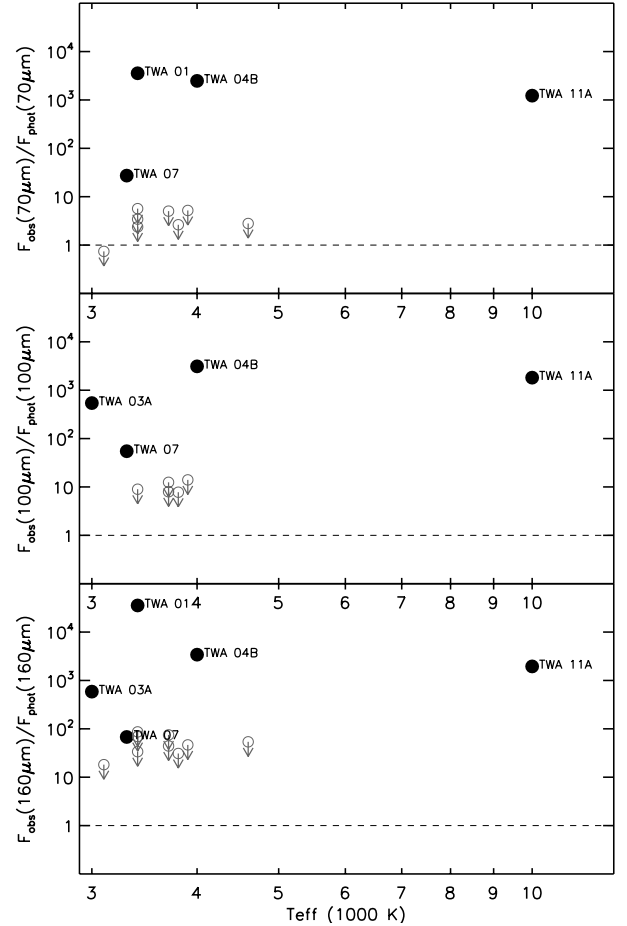


Fig. 4. Excesses at 70 (top), 100 (middle) and 160 (bottom) μm band versus T_{eff} . Solid dots represent true detections, while empty circles with arrows represent upper limits. The black horizontal dashed line shows the limit for photospheric emission. Displayed upper limits are 3σ.

100 and 160 μm. The bimodal distribution of excesses seen at 24 μm and lower mid-IR wavelengths (Weinberger et al. 2004; Low et al. 2005) is not as pronounced at 70 μm, but we note that the TWA 07 excess at 70 μm is more than one order of magnitude

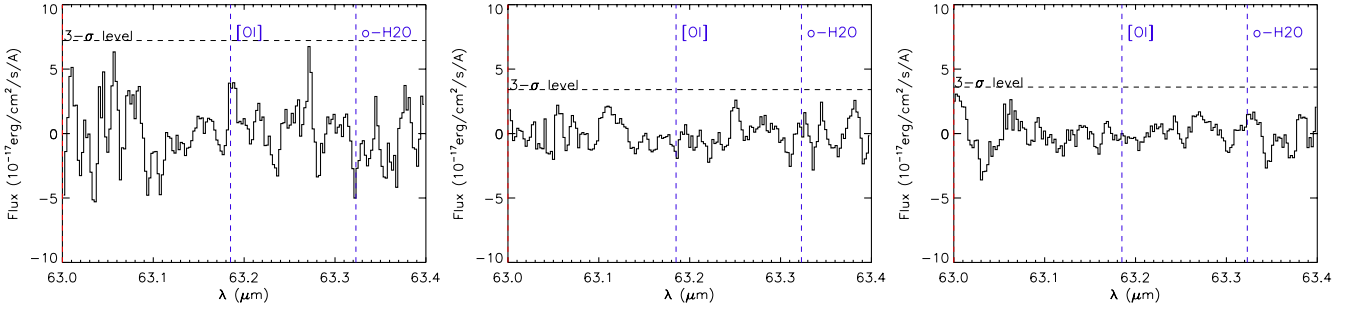


Fig. 5. Continuum subtracted spectra of TWA members showing IR excess but no line emission at 63 μm . The vertical blue dashed lines represent the position of the [OI] and o-H₂O. From left to right, targets are: TWA 03A, TWA 07 and TWA 11A. We show 3 σ limits as horizontal, black dashed lines.

smaller than any other detected excess in TWA, and that upper limits at 70 μm are near photospheric values, so probably no disc emission is present at this wavelength for those undetected sources. The bimodal nature of the distribution vanishes at 100 and 160 μm ; excesses at 100 and 160 μm cover three orders of magnitude, with ratios of the order of 10, 100 and 1000 depending on the star. Upper limits are far from the photospheric value at 100 μm , where typical values are 10 times larger than the photosphere. Finally upper limits at 160 μm are 10 to 100 times larger than the photospheric flux densities. Therefore, we can not exclude the presence of faint, cold discs in those targets.

In order to check for spatially resolved sources, we calculated azimuthally averaged radial profiles in all three PACS bands for every detected object and compared the results with the azimuthally averaged radial profile of a model point spread function (PSF) from the calibration star α Boo. We obtained the radial profiles making use of the IRAF task *pradprof*. Within the errors, none of the sources is extended in any of the PACS bands.

4.2. Herschel-PACS spectroscopy

Among the nine TWA members observed with PACS in spectral line mode, we only detected the continuum level at 63 and 189 μm in four sources, namely TWA 01, TWA 03A, TWA 04B and TWA 11A, i.e., those objects detected also with PACS photometry with the exception of TWA 07, whose spectroscopic continuum level is below the detection limit.

Only two TWA members show [OI] emission at 63.18 μm ; TWA 01 and TWA 04B. Line fluxes are given in Table 4. We note that [OI] line emission in TWA 01 was studied and modelled by Thi et al. (2010) in detail. Continuum subtracted spectra for TWA members showing IR excess with no line detections at 63 μm are shown in Fig. 5. To compute lines fluxes and upper limits, we fitted a second order polynomial to the baseline to subtract the continuum.

TWA 04B was observed at two different epochs. The resulting continuum subtracted spectra are shown in Fig. 6. The first one (OBSID 1342199409) shows a clear 3 σ detection, irrespective of the region used to compute the continuum. The second one is not as robust; it is a 3 σ detection if we exclude the noisy region that goes from 63.36 to 63.40 μm (shaded in green in Fig. 6) from the continuum computation. But if we include this region, it is at the limit of a 3 σ detection. The average spectrum shows a 3 σ detection independently of the region used to derive the continuum, so we consider that this is a real detection. Due to a shift in the line center in both observations with respect to the rest frame wavelength of [OI] (63.185 μm), the combination

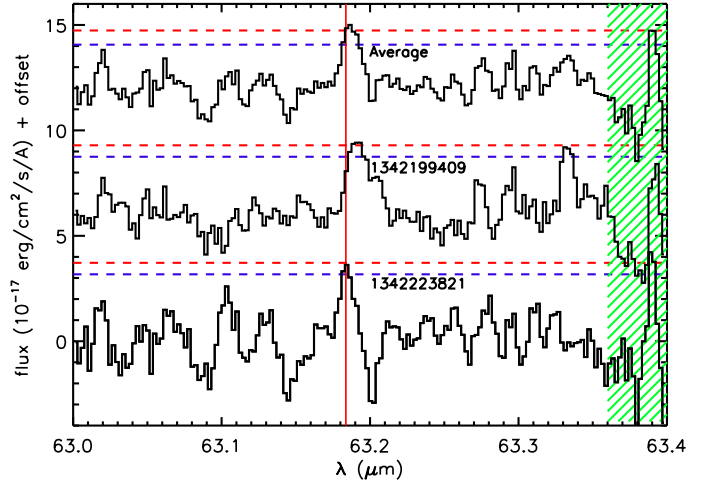


Fig. 6. The three different continuum subtracted spectra in the region around 63 μm for TWA 04B. An arbitrary vertical shift was applied to the spectra for easy comparison. The vertical red line shows the rest wavelength of the [OI] 63.18 μm emission line. The green dashed area shows the position of a region where the noise dominates the emission. The red dashed horizontal lines show the the 3 σ limit for the three spectra. The blue dashed horizontal lines show the 3 σ limit when points inside the green dashed area are excluded.

of the two epochs does not result in the expected increase in S/N. The [OI] detection in TWA 04B will be discussed further in Sect. 6.3.

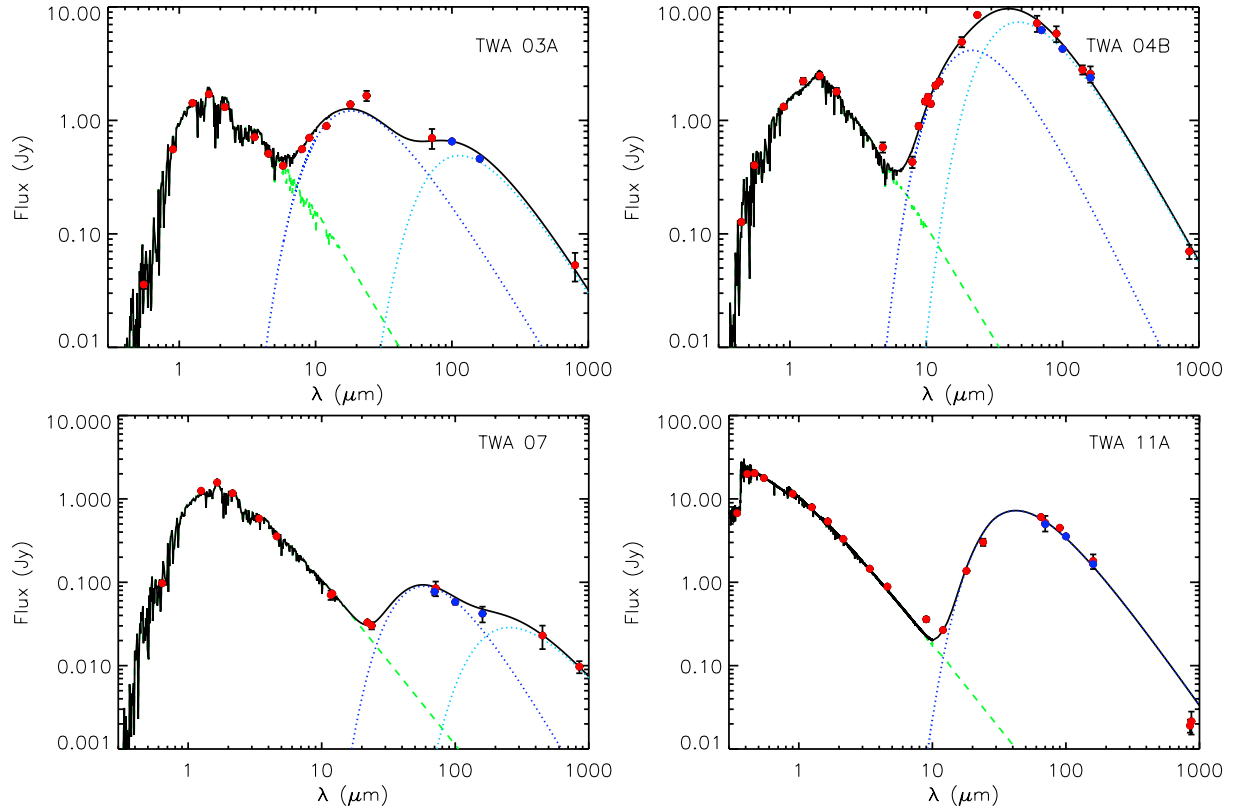
5. Models of dust discs

For every star in the sample, we built the SED including the new *Herschel*-PACS data and aiming to compare the observed data with modified blackbody models to estimate basic dust properties in the TWA association. We are aware that this approach may be very simplistic for some of these targets, but it is a good starting point for estimating dust temperatures. In any case, each individual object is discussed in the next sections. Figure 7 includes SEDs for TWA members detected with *Herschel*. The disc models were built using the NextGen models from Sect. 2.1 plus a modified blackbody to describe the dust emission, defined as

$$F_{\text{continuum}} = B_{\nu}(T_{\text{dust}}) \times (\lambda_0/\lambda)^{\beta} \quad (1)$$

Table 5. Photosphere plus modified blackbody fitting and disc parameters.

Name	T_1	β_1	T_2	β_2	L_{IR}/L_*	$R_{\text{in},1}$	$R_{\text{in},2}$	$M_{\text{dust},160\ \mu\text{m}}$	$M_{\text{dust},\text{submm}}$
–	(K)	–	(K)	–	–	(AU)	(AU)	(M_\odot)	–
TWA 03A	280 ± 5	$0^{+0.06}$	45 ± 4	$0^{+0.09}$	9.8×10^{-2}	0.416 ± 0.015	16.1 ± 5.8	0.133 ± 0.042	0.384 ± 0.159
TWA 04B	190 ± 10	0.72 ± 0.55	102 ± 2	0.185 ± 0.023	2.4×10^{-1}	4.8 ± 1.0	7.9 ± 1.6	0.259 ± 0.029	0.256 ± 0.064
TWA 07	66 ± 5	0.86 ± 0.23	20 ± 2	$0^{+0.1}$	2.2×10^{-3}	38 ± 10	75 ± 15	0.022 ± 0.011	0.146 ± 0.045
TWA 11A	108 ± 5	$0.3^{+0.2}_{-0.1}$	–	–	4.6×10^{-3}	59 ± 19	–	0.271 ± 0.109	0.146 ± 0.042


Fig. 7. Blackbody models for TWA members. Dark and light blue dashed lines depict the different blackbody components for the two blackbodies model. The blue dots represent PACS observations at 70, 100 and 160 μm . The green line represents the photospheric contribution.

with $\lambda_0 = 2\pi a_{\text{min}}$ and $\beta = 0$ for $\lambda < \lambda_0$, where B_ν is the Planck function. The choice for a_{min} depends on the target. TWA 11A is an A0 star, and therefore grains below the blow-out size (a_{blow}) are expected to be blown out from the system on timescales that are much shorter than an orbital period. Therefore, for TWA 11A $a_{\text{min}} = a_{\text{blow}}$, which can be computed using

$$\frac{a_{\text{blow}}}{1\ \mu\text{m}} = 1.15 \frac{L_*}{L_\odot} \frac{M_\odot}{M_*} \frac{1\ \text{g cm}^{-3}}{\rho}. \quad (2)$$

(Backman & Paresce 1993) with $\rho = 2.5\ \text{g cm}^{-3}$, which is valid for astrosilicates. We get $a_{\text{blow}} = 28\ \mu\text{m}$. On the other hand, TWA 01, TWA 03A, TWA 04B and TWA 07 are M stars, where no grains are expected to be blown out from the system as a result of radiation pressure. For these sources, we used $a_{\text{min}} = 0.1\ \mu\text{m}$ following the models from Augereau & Beust (2006) for AU Mic.

Both β and T_{dust} are free parameters, and β can take any value from 0 to 2. A value of 2 was found for unprocessed interstellar grains (Hildebrand 1983), while a value of 0 indicates dust grains radiating as pure blackbodies. Miyake & Nakagawa (1993) demonstrated that grain growth results in β values that are significantly lower than the standard interstellar medium (ISM) value of 2 and that grain distributions with $a_{\text{max}} \gtrsim 1000\ \mu\text{m}$

result in $\beta < 1$. Therefore, the β value from the modified blackbody fit gives us some information about the grain size distribution in TWA discs.

The best model was determined through χ^2 minimisation, with

$$\chi^2 = \frac{1}{\nu} \sum_{i=1}^N \frac{(F_{\text{obs},i} - F_{\text{mod},i})^2}{\sigma_i^2} \quad (3)$$

where N is the total number of photometric points used in the fitting, $\nu = N - n$ the degrees of freedom, n the number of free parameters, $F_{\text{obs},i}$ the observed flux density of the i th photometric point, $F_{\text{mod},i}$ the i th model flux density, and σ_i is the error of the i th photometric point. We used a genetic algorithm to search the models that minimise χ^2 . Basically, a range (minimum and maximum) for each parameter must be supplied to the algorithm, which follows these steps: 1) generate a random population of N individuals (i.e., sets of parameters, with N being user-defined and usually between 10 to 40) within the range limits for every parameter to fit; 2) generate the models corresponding to the random individuals; 3) select the best 10% of individuals based on a χ^2 minimisation; and 4) use this selection of best models to generate the next population of individuals with values in the

range -20% to $+20\%$ of the model parameters from step 3. The process is iteratively repeated until a stable point is reached, i.e., when the best χ^2 does not change more than 1% with respect to the best value on the previous generation. At this point, a random population of $10 \times N$ new individuals is added to destabilise the achieved minimum owing to avoid local minima. This process is then repeated ten times. Hence, the final value must remain stable during more than 100 generations with ten inclusions of $10 \times N$ random points in the whole parameter space. Moreover, the random population of $10 \times N$ created every time a stable point is reached is used to compute the final errors in the parameters and to check for possible multi-valued solutions. In particular, we measure the 90% contours with respect to the best χ^2 value obtained by the genetic algorithm.

From these fits, we get estimates of the dust temperature and IR excess. This analysis is useful since it relies on very few assumptions and allows easy comparison with other studies. For the sources with no IR excess detected we compute upper limits for the IR excesses by considering the flux density upper limits as detections. For TWA 01, TWA 03A, TWA 04B and TWA 07, the SED is reproduced better using two blackbodies instead of only one. That we need two blackbodies to reproduce the emission could be pointing to the presence of two populations of grains at different radii or could be the signpost of a complex system. For TWA 11A, the inclusion of a second blackbody does not result in a big improvement. Results of the fitting process are listed in Table 5, and model SEDs can be found in Fig. 7.

Using the dust temperature from the blackbody models, we can estimate the inner radius of the disc using

$$R_{\text{in}} > \frac{1}{2} R_* \left(\frac{T_*}{T_{\text{dust}}} \right)^{(4+\beta)/2}. \quad (4)$$

(Beckwith et al. 1990). Furthermore, we can estimate the dust mass in the disc by using the following expression, which is valid for optically thin discs:

$$M_{\text{dust}} = \frac{F_{\nu}(\lambda_0) D^2}{\kappa_{\nu} B_{\nu}(T_{\text{dust}})} \quad (5)$$

where D is the distance to the star, $B_{\nu}(T_{\text{dust}})$ can be approximated by the Rayleigh-Jeans regime, $\kappa_{\nu} = 2 \times (1.3 \text{ mm}/\lambda)^{\beta} \text{ cm}^2 \text{ g}^{-1}$ (Beckwith et al. 1990), and $F_{\nu}(\lambda_0)$ is the integrated flux density at a given wavelength emitting at the Rayleigh-Jeans regime. Considering that for some targets, the far-IR and sub-millimetre flux densities seem to arise from different radii, we computed dust masses using the PACS flux density at $160 \mu\text{m}$ and a sub-millimetre flux density from the literature. Disc radii and dust masses are shown in Table 5.

6. Gas and dust content in TWA circumstellar discs

We have analysed the main results from our blackbody (BB) dust models and the *Herschel* spectroscopic data. In the following, we discuss the individual sources.

6.1. TWA 01

PACS observations of TWA 01 from the GASPS programme have been previously studied and modelled in detail by Thi et al. (2010), where they modelled the circumstellar dust with a total dust mass of $\sim 63 M_{\oplus}$. Bergin et al. (2013) report detecting hydrogen deuteride (HD), and derived a gas mass $> 1.8 \times 10^5 M_{\oplus}$, high enough to form a planetary system at the age of 10 Myr.

As shown in Sect. 2.2, TWA 01 is the strongest accretor among the sample. The blackbody model for TWA 01 produces a poor fit, especially when compared with other TWA members such as TWA 04B, TWA 07, and TWA 11A. This is due to the more complex spatial distribution of dust around TWA 01 and to its optical thickness. We refer the reader to the paper by Thi et al. (2010) for a more detailed analysis of this source.

6.2. TWA 03A

Andrews et al. (2010) performed high-resolution observations of the thermal continuum emission towards TWA 03A at $880 \mu\text{m}$ with SMA. By modelling the $880 \mu\text{m}$ flux visibility and the SED, they deduced $R_{\text{out}} \sim 15\text{--}25 \text{ AU}$ (the expected radius if the disc around TWA 03A is truncated by TWA 03B), $R_{\text{in}} \sim 0.4 \text{ AU}$, and a dust mass of $2.3 M_{\oplus}$.

The best model for TWA 03A needs a population of hot grains ($T = 280 \text{ K}$) at $\sim 0.4 \text{ AU}$ to reproduce the mid-IR emission and a second population of cold grains ($T = 40 \text{ K}$) at 16 AU . We note that the model fails to reproduce the MIPS observation at $24 \mu\text{m}$. The flux density at $160 \mu\text{m}$ is not at the Rayleigh-Jeans regime, and therefore the mass computed using this flux density is a lower limit. A more realistic value for the dust mass can be obtained if the flux density in Eq. (5) is the James Clerk Maxwell Telescope (JCMT) flux density at $800 \mu\text{m}$ from Jensen et al. (1996). We get $\sim 0.38 M_{\oplus}$, about six lower smaller than the value by Andrews et al. (2010).

Muzerolle et al. (2000) studied H_{α} emission in TWA 03A and concluded that there is ongoing gas accretion in the system about one order of magnitude larger than the average value for discs in Taurus. Huenemoerder et al. (2007) studied the soft X-ray emission from the star and concluded that the shape of the spectrum was attributable to accretion shocks. The compilation of TWA 03A H_{α} equivalent widths by Barrado y Navascués (2006) shown in Fig. 2 also agree with ongoing accretion as pointed out in Sect. 2.2. This contrasts with the non-detection of [OI] emission at $63 \mu\text{m}$ and is discussed in Sect. 7.2.

6.3. TWA 04B

TWA 04B is part of a peculiar quadruple system, which is two spectroscopic binaries A and B orbiting each other. The system shows a prominent IR excess attributed to a circumbinary disc around the B pair (Koerner et al. 2000; Prato et al. 2001; Furlan et al. 2007), where both stars are separated by $\sim 1 \text{ AU}$. Skinner et al. (1992) reported the detection of a silicate emission feature around $10 \mu\text{m}$, and indicated the presence of grains as small as $0.01 \mu\text{m}$.

Different studies have modelled the IR emission in TWA 04B in the past, showing inner radii ranging from 2 AU to 5 AU and outer radii in the range from 10 to 18 AU . Some of these studies modelled the SED of TWA 04B using a complex geometry with two discs (Akeson et al. 2007; Furlan et al. 2007; Andrews et al. 2010). The most recent work by Andrews et al. (2010) suggests an outer radius of $10\text{--}15 \text{ AU}$ based on SMA observations at $880 \mu\text{m}$ and models the SED with an inner disc extending from 2 to 3.5 AU , and a second one extending from 3.5 to $\sim 15 \text{ AU}$.

Our best model for TWA 04B consists of a population of dust grains at 180 K placed at 4.8 AU and a second population of dust grains at 102 K placed at 7.9 AU from the star, with a total dust mass of $\sim 0.26 M_{\oplus}$. Our deduced radius for the inner disc is compatible within the errors with the value proposed by Andrews et al. (2010) while the radius of the outer disc is larger

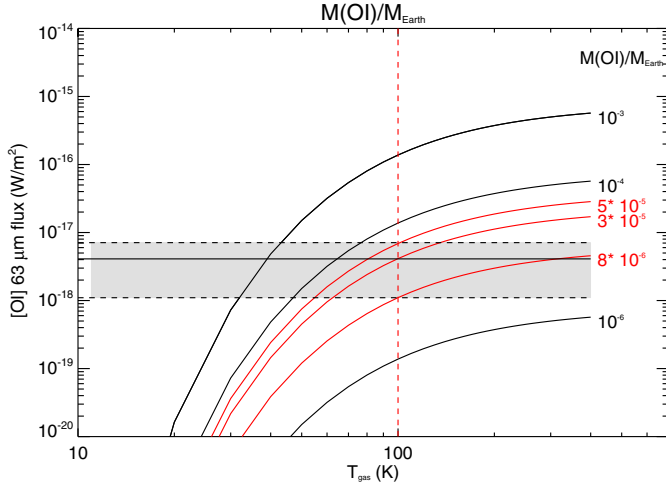


Fig. 8. Line luminosity versus gas excitation temperature for TWA 04B. The black and red curves represent the behaviour for different gas masses. The red ones show masses compatible with the observed flux range in TWA 04B for $T_{\text{gas}} = 100$ K. The grey dashed region shows the flux density values consistent with our observations.

in our model. Our dust mass is two times higher than the value by Nilsson et al. (2010), but we note that they used a single blackbody at 155 K to model the whole SED. Also, their flux density at $870 \mu\text{m}$ is lower than flux densities at similar wavelengths from the literature.

Since we detected the [OI] emission in this system, we can study the gas content of the disc. In Fig. 8, we show the line luminosity versus the excitation temperature for different gas masses. Assuming an excitation temperature of ~ 100 K for the [OI] line at $63.18 \mu\text{m}$, we can constrain the atomic oxygen gas mass to be between $8.0 \times 10^{-6} M_{\oplus}$ and $5.0 \times 10^{-5} M_{\oplus}$. Assuming a primordial gas abundance for oxygen, i.e. 8.5×10^{-4} with respect to H nuclei, the total gas mass ranges from $9.5 \times 10^{-3} M_{\oplus}$ to $6.0 \times 10^{-2} M_{\oplus}$, implying a gas-to-dust ratio that ranges roughly from 3.6×10^{-2} to 0.23. We note that, depending on the origin of the gas, the oxygen abundance can be larger, resulting in even lower gas masses and gas-to-dust ratios. Thus, we are detecting gas in a very low ratio to dust, so the system seems to be in a very advanced evolutionary stage. We can compare the OI gas detection in TWA 04B with those in TWA 01 (Thi et al. 2010) and HD172555 (Riviere-Marichalar et al. 2012a), because they share similar evolutionary stages (the general agreement is that the β Pictoris moving group is slightly older than TWA, with an absolute age in the range 12 to 20 Myr), although we must caution that HD 172555 has a very different spectral type (A0 versus M). The result of this comparison is shown in Table 6. TWA 04B shows the lowest ratio with respect to the $70 \mu\text{m}$ continuum emission. The gas in TWA 01 is probably primordial, while some authors (Lisse et al. 2009; Johnson et al. 2012) argue that the gas in HD 172555 comes from the sublimation of silicates (olivines, pyroxenes) in hypervelocity collision. Considering the low line-to-continuum flux ratio in TWA 04B when compared with TWA 01, we suggest that the gas should have a second-generation origin, possibly from cometary evaporation.

Soderblom et al. (1996) proposed a chromospheric origin for the H_{α} emission, as we did in Sect. 2.2. Dent et al. (2005) did not detect CO emission in TWA 04B. That TWA 04B shows [OI] in emission at $63 \mu\text{m}$ while showing no accretion would be pointing to a disc with an inner gap empty of gas, but with measurable amounts of gas at a larger radius. The origin of the gap may

Table 6. Gas detections in TWA and β Pictoris moving group (BPMG).

Target	$\frac{F_{[\text{OI}]}}{\lambda_{70 \mu\text{m}} \times F(\lambda_{70 \mu\text{m}})}$	M_{dust}	M_{gas}
—	—	M_{\oplus}	M_{\oplus}
TWA 04B	1.5×10^{-5}	0.26	$(0.95-6) \times 10^{-2}$
TWA 01	2.2×10^{-4}	63	160–1600
HD 172555	5.5×10^{-3}	4.8×10^{-4}	4.8×10^{-41}
TWA 03A	$<2.0 \times 10^{-4}$	0.38	$<0.042^2$
TWA 07	$<1.3 \times 10^{-3}$	0.15	$<0.027^2$
TWA 11A	$<2.1 \times 10^{-5}$	0.15	$<0.082^2$

Notes. ⁽¹⁾ Atomic oxygen mass only, see Riviere-Marichalar et al. (2012a). ⁽²⁾ Computed assuming primordial gas abundance for oxygen, i.e. 8.5×10^{-4} with respect to H-nuclei.

be related to the binary nature of the system, with separation of ~ 1.0 AU.

6.4. TWA 07

TWA 07 is an M1 star (Webb et al. 1999) placed at 38 pc from the Sun. Low et al. (2005) used MIPS observations to study dust emission in TWA 07 and modelled the SED with an 80 K blackbody at 6.8 AU from the star and with a minimum mass of $\sim 4 \times 10^{-5} M_{\oplus}$. Later on, Matthews et al. (2007) observations at 450 and $850 \mu\text{m}$ demonstrate that dust in a range of temperatures is needed to fit the $24 \mu\text{m}$ and the sub-millimetre flux densities simultaneously.

Fitting TWA 07 with a single blackbody model results in a poor fit, while including a second blackbody highly increases the quality of the fit. The best model consists of an inner disc at 66 K, with $\beta = 0.86$ placed at ~ 38 AU from the star, and a second, very cold blackbody (20 K) at ~ 75 AU from the star. This is the coldest disc among the sample, and it is more than two times cooler than the Sun’s Edgeworth-Kuiper belt, at ~ 45 K. As pointed out by Matthews et al. (2007), no single temperature can fit both the near and mid-IR and the sub-millimetre flux densities. Including the $160 \mu\text{m}$ PACS photometric point pushes the outer blackbody to cooler temperatures and clearly demonstrates the bimodal shape of the SED. We are aware that the combination of many different grain size distributions can result also in a bimodal shape (see Matthews et al. 2007), but we consider the presence of dust at different radii as the most plausible explanation. Because the flux density at $160 \mu\text{m}$ will underestimate the dust mass, we deduced a value of $0.15 M_{\oplus}$ using the flux density at $870 \mu\text{m}$ by Matthews et al. (2007).

According to Sect. 2.2, the H_{α} equivalent width agree with no ongoing accretion in TWA 07. The PACS line spectrum of this source does not show line emission. Both facts agree with an evolved, second-generation debris disc.

6.5. TWA 11A

Infrared excess around TWA 11A was reported for the first time by Jura (1991), who highlighted the prominence of this excess when compared with β Pictoris. Jura et al. (1993) studied the TWA 11A SED, and proposed a typical size of $10 \mu\text{m}$ for dust grains located at 40 AU from the star. Koerner et al. (1998) showed that the morphology of the emission at $20.8 \mu\text{m}$ agrees with a ring-like structure extending from 55 to 85 AU, while the excess at $12.5 \mu\text{m}$ arises predominantly from the region inside this radius, from gravitationally confined grains. Resolved

images of the disc have been studied by several authors (Koerner et al. 1998; Jayawardhana et al. 1998; Schneider et al. 1999; Telesco et al. 2000), who agree that the detected emission should arise from material at least at 55 AU. Augereau et al. (1999) modelled the SED with an outer disc at ~ 70 AU and an inner disc at ~ 9 AU, with a total solid mass of $\sim 3.9 M_{\oplus}$ in a grain size distribution with $a_{\max} = 100$ cm. Since the dust mass is $M_{\text{dust}} \propto a_{\max}^{0.5}$ in this model, the dust mass in grains < 1 mm is $\sim 0.11 M_{\oplus}$.

For TWA 11A, including a second blackbody in the model does not result in a big improvement, so we kept a single blackbody model as the best option. The dust temperature is 108 K, corresponding to a disc at 59 AU, in good agreement with previous results with $\beta = 0.3$. If we use the $160 \mu\text{m}$ flux density to derive the dust mass we get $M_{\text{dust}} = 0.27 M_{\oplus}$, only two times the mass deduced by Augereau et al. (1999), a difference that can be considered satisfactory given the uncertainties associated with the dust opacity law. We note that the model overestimates the observed intensity at sub-millimetre wavelengths. A dust mass of $\sim 0.146 M_{\oplus}$ was then computed using the flux density at $870 \mu\text{m}$ by Nilsson et al. (2010), which agrees even better with previous results.

TWA 11A does not show [OI] emission at $63 \mu\text{m}$. The lack of atomic emission in TWA 11A has already been reported and discussed in the study of atomic and molecular emission in the GASPS sample of HAeBe stars by Meeus et al. (2012). The authors show how other stars with similar spectral types emit in [OI] at $64.18 \mu\text{m}$ (e.g. AB Aur, HD 97048). Therefore the lack of [OI] emission towards TWA 11A cannot be attributed to its spectral type. But we caution that discs around AB Aur and HD 97048 are protoplanetary, gas-rich systems. Therefore, the lack of [OI] is not linked to the spectral type, but to the evolutionary stage of the system.

7. Discussion

TWA members detected with PACS show a wide variety of dust and gas properties from TWA 01, harbouring a protoplanetary-like disc with strong gas emission and ongoing active gas accretion, to TWA 07, which seems to be devoid of gas but shows two debris rings at different radii. TWA 04B is considered a transitional disc, and it shows no accretion according to its H_{α} emission, but shows [OI] in emission at $63.18 \mu\text{m}$. Inner radii span a wide range of values, from ~ 0.4 AU for TWA 03A to 59 AU for TWA 11A, independent of the spectral type. The wide variety of properties in the five TWA discs studied most likely indicates that there are several factors driving disc evolution, and not just the age, including the dust/gas initial mass, the mass of the central object, angular momentum, multiplicity, composition of the original cloud, and possibly planet formation itself. Other authors have arrived at the same conclusion (Furlan et al. 2006; Bayo et al. 2012; Lada et al. 2006; Hernández et al. 2007; Currie & Sicilia-Aguilar 2011).

7.1. Dust in TWA

TWA 01 shows the highest dust mass in the sample, $\sim 63 M_{\oplus}$ (Thi et al. 2010, including PACS observations from GASPS), while other TWA members studied in the present work show dust masses in the range 0.15 to $0.38 M_{\oplus}$. According to our numbers, except for TWA 01, there is no mass left to form planets within the TWA members studied. The same result for a partially

overlapping TWA sample was already reported by Weinberger et al. (2004). Furthermore, we find no correlation between the spectral type and the dust mass; TWA 11A and TWA 07, which are A0 and M1 stars respectively, have approximately the same dust mass. On the other hand, TWA 01, which is an M2.5 star, shows a mass that is ~ 400 times larger than TWA 07 mass.

Another interesting point is the fact that TWA 11A, which is an A0 star (Barrado y Navascués 2006), does not show gas emission, while showing a very prominent IR excess. The disc is clearly a second generation debris disc, while TWA 01, TWA 03A and TWA 04B show SEDs that resemble those of transitional discs. This result agrees with the hypothesis that discs around early type stars tend to evolve faster toward the debris phase than late type stars. We note that we only have one early spectral-type object, and therefore this conclusion has to be taken with some caveats.

The β values in the outer discs are typically around 0 (pure blackbody emission), with an average value of $\beta_2 = 0.12$, which implies grains with sizes of the order of $\sim 1000 \mu\text{m}$ (Draine 2006), so significantly larger than ISM grains. This may be indicative of a second-generation origin for dust grains, but also may be a signpost of grain growth. On the other hand, β values for inner discs have an average value of $\beta_1 = 0.53$, i.e., similar to those values found for T Tauri stars in Taurus-Auriga (Mannings & Emerson 1994, with a typical value of 0.6). This illustrates the need for populations with different sizes at different radii.

The PACS detections in TWA can help us understand some evolutionary trends in the transition from a protoplanetary disc to a debris disc. The first is that all the detected objects in TWA show large IR excess, as already reported by Low et al. (2005) using *Spitzer* data. There are no detections of weak excesses in the sample. This may suggest that the dust (and gas) depletion rate is faster than the replenishment rate by collisions between planetesimals from an unseen population. If discs are formed with an initially low gas and dust content, it may be that large planetesimals never formed. On the other hand, the high-mass objects detected in this survey may be those with enough initial gas and dust that a significant population of planetesimals exist.

Donaldson et al. (2012) have recently modelled the SED of some Tuc Hor members that were also part of the GASPS sample and concluded that all the detected discs were debris discs, with no [OI] emission. In the present study, we have detected five discs in TWA, but they span a wide range of disc parameters, including both debris discs and protoplanetary discs. Tuc Hor is a 30 Myr old association, while TWA is significantly younger (8 to 20 Myr, depending on different authors). The different range in ages can explain not only the presence of protoplanetary/transitional systems in TWA, but also the fact that we detect [OI] emission at $63 \mu\text{m}$ in two systems (namely TWA 01 and TWA 04 B), while no [OI] emission is observed in Tuc Hor.

7.2. Gas in TWA

There are some interesting questions regarding the gas content in TWA member discs. The [OI] detection in TWA 01 (TW Hya) was studied in detail in Thi et al. (2010), where they estimated a gas mass of 160 to $1600 M_{\oplus}$. This mass is four to six orders of magnitude higher than the mass that we estimated for TWA 04 B. If we estimate the gas mass for TWA 01 in the same way as we did for TWA 04B, we get a mass in the range 0.3 to $0.6 M_{\oplus}$, so much lower than the more realistic value by Thi et al. (2010), but again 5 to 61 times higher than the gas mass in TWA 04B.

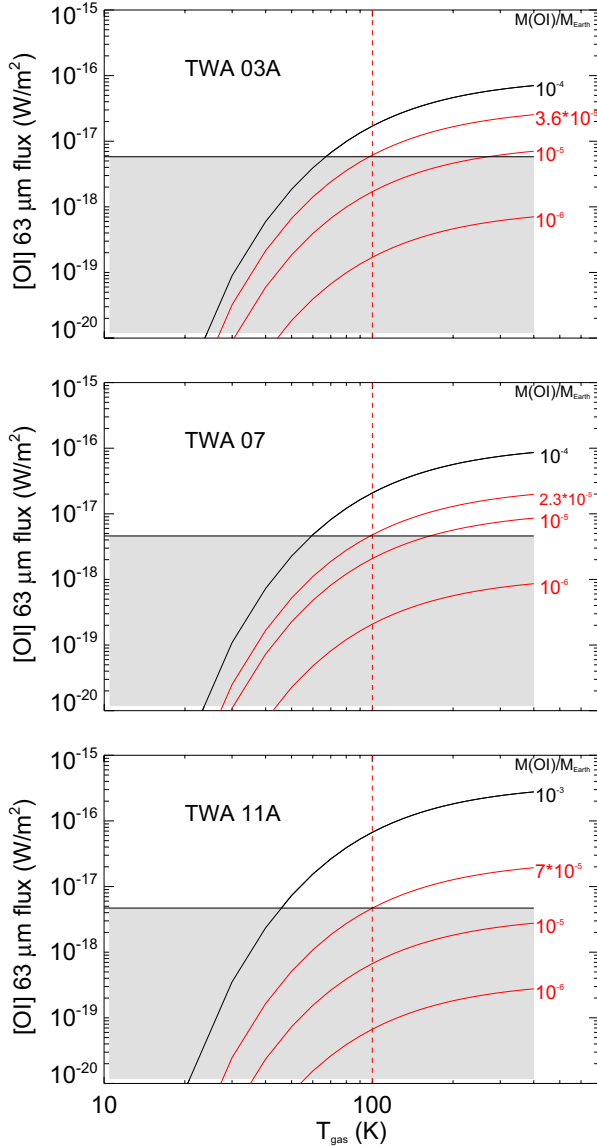


Fig. 9. Line luminosity versus gas excitation temperature for TWA members with no [OI] emission detected. The black and red curves represent the behaviour for different gas masses. The red ones show masses compatible with the flux upper limits for $T_{\text{gas}} = 100$ K. The grey dashed region shows the parameter space compatible with observations.

Both stars have similar spectral-types: M2.5 for TWA 01 (Vacca & Sandell 2011) and M5 for TWA 04B (Gregorio-Hetem et al. 1992). Given that the spectral types are so similar, what is driving the large difference in gas mass? One possibility is that the difference comes from the size of the disc, therefore the total initial mass available. The disc in TWA 04B is truncated by the primary, TWA 04A, at ~ 15 AU, while TWA 01 is expected to be much more extended (196 AU, Qi et al. 2004). Also, TWA 04B is itself a close spectroscopic binary, which opens a large inner gap devoid of gas and dust; therefore, the difference in dust and gas evolution can also be related to multiplicity.

In Fig. 9 we show [OI] luminosity at $63 \mu\text{m}$ versus the excitation temperature for objects not detected with PACS at $63.18 \mu\text{m}$. As can be seen, upper limits on the [OI] gas mass are a few $10^{-5} M_{\oplus}$, which is similar to the [OI] gas mass in TWA 04B.

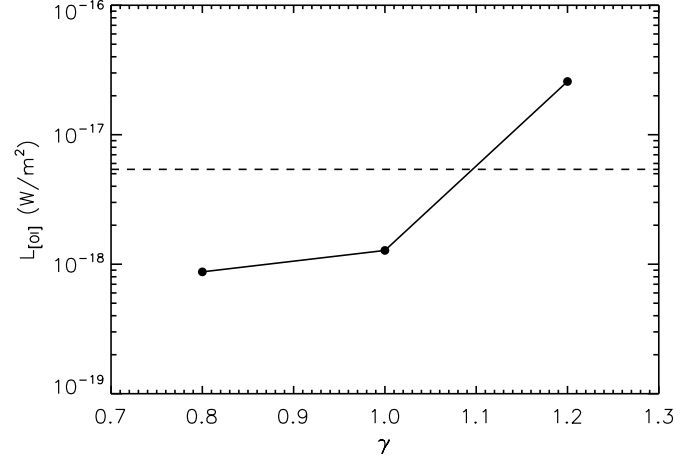


Fig. 10. [OI] luminosity at $63.18 \mu\text{m}$ versus flaring index (γ) for a model star with $L_* = 0.13 L_{\odot}$, $R_{\text{in}} = R_{\text{sub}}$, $R_{\text{out}} = 100$ AU, $a_{\text{min}} = 0.05 \mu\text{m}$, $a_{\text{max}} = 1000 \mu\text{m}$, $\epsilon = -1.0$, $f_{\text{UV}} = 0.1$ and $M_{\text{dust}} = M_{\text{gas}} = 10^{-6} M_{\odot}$ at the distance of TWA 03A. The model is for illustration, and is not intended to represent TWA 03A exactly, but a generic system with similar stellar parameters. The horizontal, dashed line represents the average upper limit for objects in TWA.

The gas mass in TWA 01 is therefore more than one order of magnitude higher than any other gas mass in the association.

It is also interesting to compare the detection of [OI] gas in TWA 04B with the non-detection in TWA 03. In Sect. 2.2 we classified TWA 03 as an accreting disc and TWA 04B as a non-accreting disc. The [OI] gas detection combined with the absence of accretion in TWA 04B can be explained by the fact that TWA 04B is a close spectroscopic binary, and therefore no gaseous material could survive inside 1 AU, and no accretion could be detected (see Prato et al. 2001). Our own determination of the inner radius in TWA 04B agrees with an inner hole > 1 AU.

That that we do not detect any [OI] emission in TWA 03A while we see signs of accretion is intriguing. A possible explanation relies on the geometry of the disc. If the disc is very flat, then there is not enough material irradiated by the central star, small amounts of oxygen are excited, and the resulting [OI] emission should be too weak to be detected. We do not claim that this is the only possible explanation. A lower ultraviolet (UV) flux could also explain the difference between TWA 03A and TWA 04B, since the UV flux is the main source of energy for the gas heating via photoelectric effects on dust grains and polycyclic aromatic hydrocarbons. However, both targets are a similar spectral type so we expect that the UV flux is very similar. Indeed, TWA 03A is actively accreting, and therefore we expect a higher UV flux from that source, so a difference in the flaring geometry is the most plausible explanation for the difference in [OI] emission. In Fig. 10 we represent the [OI] luminosity at $63.18 \mu\text{m}$ versus the flaring index (γ) for a model system taken from the DENT grid of models (Kamp et al. 2011) scaled to the distance of TWA 03A, 42 pc. As can be seen, the flux for the same star dramatically changes by more than one order of magnitude by changing the flaring index, in such a way that only the system with $\gamma = 1.2$ could be detected by our PACS observations, while all of them share the same gas and dust mass. Overall, Fig. 10 shows that in discs with low-mass gas, hence a low mass-accretion rate, OI is very difficult to detect with current instrumentation.

In Taurus, 46 stars with discs out of 76 observed show [OI] emission (Howard et al. 2013), while in TWA we

detected line emission in two systems out of the nine observed and in two out of the five known to have discs. Although the number of observations or detections in TWA is too low to make statistical arguments, we highlight the difference in gas-rich discs fractions from Taurus (0.6) to TWA (0.4). Riviere-Marichalar et al. (2012b) showed that warm water emission is commonly found among Taurus T Tauri stars, but we do not detect warm water emission toward TWA members; while ~24% of the gas-rich Taurus members (i.e., those showing [OI] emission at 63 μm) show water emission at 63.32 μm , no TWA members show water emission at 63 μm . According to Riviere-Marichalar et al. (2012b), the water emission around T Tauri stars in Taurus comes from a region at ~1 AU and ~3 AU wide. TWA 04B, TWA 07, and TWA 11A show inner radii larger than 3 AU, therefore no water could be detected in the regions. For TWA 01 and TWA 03A, the lack of warm water emission must have a different explanation, most probably one related to reprocessing of circumstellar gas or the geometry of the discs.

8. Summary and conclusions

We observed 14 TWA members with the PACS instrument on board the *Herschel* Space Observatory. All of them were observed with the PACS photometer (70, 100, and/or 160 μm). Nine were observed with PACS Line Spectroscopy, targeting [OI] at 63 μm . The main conclusions are the following:

1. We detected excess photometric emission at 70 μm , 100 μm and 160 μm in 4, 4 and 5 systems out of 12, 9 and 14 observed at these wavelengths. We detected for the first time 100 μm and 160 μm emission towards TWA 07, and also 100 μm emission towards TWA 03A. Objects not detected at 70 μm show upper limits near the photospheric level. Therefore, if present, any circumstellar material must be cold or very low mass.
2. Among the five systems detected with IR excess, two of them (TWA 01 and TWA 04B) show [OI] emission at 63.18 μm , indicating the presence of gas in those systems. None of the systems show water emission at 63.32 μm . Future research is needed to understand the gas emission in TWA 04B.
3. We modelled the dust IR emission with blackbody models, and used them to derive dust masses and inner radii, thereby providing temperatures in the range 20 (TWA 07) to 280 K (TWA 04B). Dust masses are in the range 0.146 (TWA 07 and TWA 11A, from blackbody models) to 63 M_{\oplus} (TWA 01, from detailed modelling). Disc radii are in the range 0.4 to 59 AU.

TWA members show a wide variety of disc properties, implying different stages of disc evolution, from the protoplanetary/transitional, gas-rich disc around TWA 01 to the very cold, gas-free debris disc surrounding TWA 07. We propose that there must be several factors (others than the age) driving the evolution of the gas and dust contents in circumstellar environments, such as multiplicity, disc mass, stellar mass, angular momentum and composition, and, in general, initial conditions.

Acknowledgements. This research has been funded by Spanish grants AYA 2010-21161-C02-02, AYA2012-38897-C02-01, AYA2011-26202 CDS2006-00070, and PRICIT-S2009/ESP-1496. We also acknowledge support from ANR (contract ANR-07-BLAN-0221) and PNPS of CNRS/INSU, France. C. Pinte acknowledges funding from the European Commission's 7th Framework programme (contract PERG06-GA-2009-256513) and from Agence Nationale pour la Recherche (ANR) of France under contract ANR-2010-JCJC-0504-01. W.F.T.

thanks the CNES for a post-doctoral position. W.F.T., F.M. and I.K. acknowledge funding from the EU FP7-2011 under Grant Agreement nr. 284405 (DIANA project). J.C.A. acknowledges the PNP-CNES for financial support. F.M. acknowledges support from the Millennium Science Initiative (Chilean Ministry of Economy), through grant "Nucleus P10-022-F".

References

- Akeson, R. L., Rice, W. K. M., Boden, A. F., et al. 2007, *ApJ*, 670, 1240
- Andrews, S. M., Czekala, I., Wilner, D. J., et al. 2010, *ApJ*, 710, 462
- Augereau, J.-C., & Beust, H. 2006, *A&A*, 455, 987
- Augereau, J. C., Lagrange, A. M., Mouillet, D., Papaloizou, J. C. B., & Grorod, P. A. 1999, *A&A*, 348, 557
- Backman, D. E., & Paresce, F. 1993, in *Protostars and Planets III*, eds. E. H. Levy, & J. I. Lunine, 1253
- Baraffe, I., Chabrier, G., Allard, F., & Hauschildt, P. H. 1998, *A&A*, 337, 403
- Barrado y Navascués, D. 2006, *A&A*, 459, 511
- Barrado y Navascués, D., & Martín, E. L. 2003, *AJ*, 126, 2997
- Bayo, A., Rodrigo, C., Barrado Y Navascués, D., et al. 2008, *A&A*, 492, 277
- Bayo, A., Barrado, D., Huélamo, N., et al. 2012, *A&A*, 547, A80
- Beckwith, S. V. W., Sargent, A. I., Chini, R. S., & Guesten, R. 1990, *AJ*, 99, 924
- Bergin, E. A., Cleeves, L. I., Gorti, U., et al. 2013, *Nature*, 493, 644
- Bryden, G., Beichman, C. A., Trilling, D. E., et al. 2006, *ApJ*, 636, 1098
- Burgasser, A. J., Kirkpatrick, J. D., Reid, I. N., et al. 2003, *ApJ*, 586, 512
- Chen, C. H., Sargent, B. A., Bohac, C., et al. 2006, *ApJS*, 166, 351
- Cieza, L. A., Swift, J. J., Mathews, G. S., & Williams, J. P. 2008, *ApJ*, 686, L115
- Currie, T., & Sicilia-Aguilar, A. 2011, *ApJ*, 732, 24
- de la Reza, R., Torres, C. A. O., Quast, G., Castilho, B. V., & Vieira, G. L. 1989, *ApJ*, 343, L61
- de la Reza, R., Jilinski, E., & Ortega, V. G. 2006, *AJ*, 131, 2609
- Dent, W. R. F., Greaves, J. S., & Coulson, I. M. 2005, *MNRAS*, 359, 663
- Dent, W. R. F., Thi, W. F., Kamp, I., et al. 2013, *PASP*, accepted
- Donaldson, J. K., Roberge, A., Chen, C. H., et al. 2012, *ApJ*, 753, 147
- Draine, B. T. 2006, *ApJ*, 636, 1114
- Furlan, E., Hartmann, L., Calvet, N., et al. 2006, *ApJS*, 165, 568
- Furlan, E., Sargent, B., Calvet, N., et al. 2007, *ApJ*, 664, 1176
- Gregorio-Hetem, J., Lepine, J. R. D., Quast, G. R., Torres, C. A. O., & de La Reza, R. 1992, *AJ*, 103, 549
- Hauschildt, P. H., Allard, F., & Baron, E. 1999, *ApJ*, 512, 377
- Hernández, J., Hartmann, L., Megeath, T., et al. 2007, *ApJ*, 662, 1067
- Hildebrand, R. H. 1983, *QJRAS*, 24, 267
- Hoff, W., Henning, T., & Pfau, W. 1998, *A&A*, 336, 242
- Houk, N., & Fuentes-Williams, T. H. 1982, in *BAAS*, 14, 615
- Howard, C. D., Sandell, G., Vacca, W. D., et al. 2013, *ApJ*, submitted
- Huenemoerder, D. P., Kastner, J. H., Testa, P., Schulz, N. S., & Weintraub, D. A. 2007, *ApJ*, 671, 592
- Jayawardhana, R., Fisher, R. S., Hartmann, L., et al. 1998, *ApJ*, 503, L79
- Jensen, E. L. N., Mathieu, R. D., & Fuller, G. A. 1996, *ApJ*, 458, 312
- Johnson, B. C., Lisse, C. M., Chen, C. H., et al. 2012, *ApJ*, 761, 45
- Jura, M. 1991, *ApJ*, 383, L79
- Jura, M., Zuckerman, B., Becklin, E. E., & Smith, R. C. 1993, *ApJ*, 418, L37
- Kamp, I., Woitke, P., Pinte, C., et al. 2011, *A&A*, 532, A85
- Kastner, J. H., Zuckerman, B., Weintraub, D. A., & Forveille, T. 1997, *Science*, 277, 67
- Koerner, D. W., Ressler, M. E., Werner, M. W., & Backman, D. E. 1998, *ApJ*, 503, L83
- Koerner, D. W., Jensen, E. L. N., Cruz, K. L., Guild, T. B., & Gultekin, K. 2000, *ApJ*, 533, L37
- Krivov, A. V. 2010, *A&AR*, 10, 383
- Lada, C. J., Muench, A. A., Luhman, K. L., et al. 2006, *AJ*, 131, 1574
- Lin, D. N. C., & Papaloizou, J. C. B. 1993, in *Protostars and Planets III*, eds. E. H. Levy, & J. I. Lunine, 749
- Lisse, C. M., Chen, C. H., Wyatt, M. C., et al. 2009, *ApJ*, 701, 2019
- Low, F. J., Smith, P. S., Werner, M., et al. 2005, *ApJ*, 631, 1170
- Makarov, V. V., & Fabricius, C. 2001, *A&A*, 368, 866
- Makarov, V. V., Gaume, R. A., & Andrievsky, S. M. 2005, *MNRAS*, 362, 1109
- Mannings, V., & Emerson, J. P. 1994, *MNRAS*, 267, 361
- Mathews, B. C., Kalas, P. G., & Wyatt, M. C. 2007, *ApJ*, 663, 1103
- Meeus, G., Montesinos, B., Mendigutía, I., et al. 2012, *A&A*, 544, A78
- Miyake, K., & Nakagawa, Y. 1993, *Icarus*, 106, 20
- Morales, F. Y., Werner, M. W., Bryden, G., et al. 2009, *ApJ*, 699, 1067
- Muzerolle, J., Calvet, N., Briceño, C., Hartmann, L., & Hillenbrand, L. 2000, *ApJ*, 535, L47
- Najita, J. R., Strom, S. E., & Muzerolle, J. 2007, *MNRAS*, 378, 369
- Nilsson, R., Liseau, R., Brandeker, A., et al. 2010, *A&A*, 518, A40

- Oliveira, I., Olofsson, J., Pontoppidan, K. M., et al. 2011, *ApJ*, 734, 51
- Pilbratt, G. L., Riedinger, J. R., Passvogel, T., et al. 2010, *A&A*, 518, L1
- Plavchan, P., Werner, M. W., Chen, C. H., et al. 2009, *ApJ*, 698, 1068
- Poglitsch, A., Waelkens, C., Geis, N., et al. 2010, *A&A*, 518, L2
- Prato, L., Ghez, A. M., Piña, R. K., et al. 2001, *ApJ*, 549, 590
- Qi, C., Ho, P. T. P., Wilner, D. J., et al. 2004, *ApJ*, 616, L11
- Rebull, L. M., Stapelfeldt, K. R., Werner, M. W., et al. 2008, *ApJ*, 681, 1484
- Riviere-Marichalar, P., Barrado, D., Augereau, J.-C., et al. 2012a, *A&A*, 546, L8
- Riviere-Marichalar, P., Ménard, F., Thi, W. F., et al. 2012b, *A&A*, 538, L3
- Salyk, C., Blake, G. A., Boogert, A. C. A., & Brown, J. M. 2007, *ApJ*, 655, L105
- Schneider, G., Smith, B. A., Becklin, E. E., et al. 1999, *ApJ*, 513, L127
- Schneider, A., Melis, C., & Song, I. 2012, *ApJ*, 754, 39
- Skinner, C. J., Barlow, M. J., & Justtanont, K. 1992, *MNRAS*, 255, 31P
- Soderblom, D. R., Henry, T. J., Shetrone, M. D., Jones, B. F., & Saar, S. H. 1996, *ApJ*, 460, 984
- Soderblom, D. R., King, J. R., Siess, L., et al. 1998, *ApJ*, 498, 385
- Stauffer, J. R., Hartmann, L. W., & Barrado y Navascues, D. 1995, *ApJ*, 454, 910
- Sterzik, M. F., Alcalá, J. M., Covino, E., & Petr, M. G. 1999, *A&A*, 346, L41
- Strom, K. M., Strom, S. E., Edwards, S., Cabrit, S., & Skrutskie, M. F. 1989, *AJ*, 97, 1451
- Telesco, C. M., Fisher, R. S., Piña, R. K., et al. 2000, *ApJ*, 530, 329
- Thi, W.-F., Mathews, G., Ménard, F., et al. 2010, *A&A*, 518, L125
- Torres, C. A. O., Quast, G. R., de La Reza, R., et al. 2003, in *Astrophys. Space Sci. Libr.*, eds. J. Lépine, & J. Gregorio-Hetem, 299, 83
- Torres, C. A. O., Quast, G. R., da Silva, L., et al. 2006, *A&A*, 460, 695
- Vacca, W. D., & Sandell, G. 2011, *ApJ*, 732, 8
- Webb, R. A., Zuckerman, B., Platais, I., et al. 1999, *ApJ*, 512, L63
- Weinberger, A. J., Becklin, E. E., Zuckerman, B., & Song, I. 2004, *AJ*, 127, 2246
- Weintraub, D. A., Saumon, D., Kastner, J. H., & Forveille, T. 2000, *ApJ*, 530, 867
- Williams, J. P., & Cieza, L. A. 2011, *ARA&A*, 49, 67
- Zuckerman, B., & Song, I. 2004, *ARA&A*, 42, 685
- Zuckerman, B., Webb, R. A., Schwartz, M., & Becklin, E. E. 2001, *ApJ*, 549, L233